European Cells and Materials Vol.47 2024 (pages 238–252) DOI: 10.22203/eCM.v047a15 ISSN 1473-2262

Original Article

MICROFLUIDIC BONE CHIP TO STUDY OSTEOGENESIS OF POROUS SUBSTRATE TOPOGRAPHIES IN NORMAL AND OSTEOPOROTIC MICROENVIRONMENTS

J. Yang[1], P. Duan[1], Q. Liu[1], H. Yu[1], F. Fang[1] and X. Liu[1,*]

[1]Institute of Biomedical Engineering, West China School of Basic Medical Sciences & Forensic Medicine, Sichuan University, 610041 Chengdu, Sichuan, China

Abstract

Natural bone is a material with a hierarchical porous structure; therefore, the pore size of bone tissue at the micro-scale is crucial for osteoblast function and osteogenesis. However, the physiological mechanisms behind pore size-regulated osteogenesis remain unclear. Trabecular separation is one of the main parameters of bone trabeculae structure, which is the gap between the trabeculae and can be understood as porosity. This study uses a bioinspired bone chip made from polydimethylsiloxane (PDMS) to mimic the multiscale microstructures of healthy and osteoporotic bone tissue based on data on trabecular separation from healthy and osteoporotic mice. Microchannels in the chip were made in the same topology and substrate but at different micro-scales. The result showed that osteoblasts seeded into the smaller microchannel (200 µm in diameter, mimicking healthy bone) demonstrate greater osteogenic capability and autophagy than in the larger one (350 µm in diameter, mimicking osteoporotic bone). In addition, changes in osteogenesis between each microchannel after using the autophagy inhibitor chloroquine (CQ) indicated that osteogenesis was accelerated by autophagy in the 200 µm microchannel. Finally, we found stronger osteogenesis in the 200 µm microchannel, which depends on the activation of Hippo/YAP signaling. This bioinspired bone chip, which mimics the cellular behavioral changes in the osteoporotic microenvironment at the tissue level during the transition from healthy to osteoporotic bone, is expected to be the ideal *in vitro* platform for studying osteoporosis (OP).

Keywords: Osteogenesis, microfluidic, bone, organ-on-a-chip, osteoporosis.

***Address for correspondence**: X. Liu, Institute of Biomedical Engineering, West China School of Basic Medical Sciences & Forensic Medicine, Sichuan University, 610041 Chengdu, Sichuan, China. Email: liuxiaohg@scu.edu.cn

Introduction

Osteoporosis (OP) is a bone disorder characterized by degradation of bone microstructure (Ensrud and Crandall, 2017). It has become usual with an increase in older people (Compston *et al*., 2019). Osteoporosis literally means "porous bone", which has long been linked to "enlarged cavities" in trabecular bone (Schapira and Schapira, 1992). That is to say, its traditional definition was related to the enlarged size of pore-channel in bone tissue. It has been recognized that bone arrangement and connectedness (architecture) changes are essential causes of OP (Parfitt, 1987). Natural bones' superiority stems from the structure's natural complexity, such as multiple pore scales (Wegst *et al*., 2015). Conventional bone chips are challenging to simulate complicated bone architectures, which hampers the ability to investigate physiological or diseased bone tissue (Mansoorifar *et al*., 2021).

Simulating the characteristics of a natural bone is not a trivial task. Even though the current cell culture strategies enable the study of cellularized and mineralized interaction on OP, it cannot approximate the native complexity of 3D bone microstructure. Hence, there is a significant need for *in vitro* chips mimicking natural bone-related functions (Zhang *et al*., 2023). Most research into bone regeneration and tumor-mediated bone damage has used the traditional *in-vivo* animal model and *in-vitro* 2D cell culturing system (Wittkowske *et al*., 2016; Yang *et al*., 2020). The traditional culture of cell protocols allows for studying cell behaviors, which is enabled by relatively inexpensive materials and easy techniques (Katt *et al*., 2016). Nevertheless, they cannot reproduce the 3D native bone microenvironment, and many dynamic cell-cell and cell-substrate interactions are required for skeletal physiologic functions (Portillo-Lara and Annabi, 2016).

Microfluidics is an emerging strategy to simulate *in-vivo* microenvironments rather than conventional 2D cell

cultures (Jiang *et al*., 2016). Microfluidics is a technique for handling or manipulating small amounts of fluid by utilizing channels with dimensions ranging from tens to hundreds of micrometers (Whitesides, 2006). Microfluidics can offer high surface volume ratios, flow shear stress, and manageable chemistry and physics gradients needed in biological microenvironments, which are unavailable in macroscale cellular research and uncontrolled in *in-vivo* investigations (Holmes and Gawad, 2010). Microfluidic modeling can reproduce bionic environments by culturing various types of cells, adjusting spatiotemporal chemistry and physics gradients, and mechanic features of the cellular microenvironments (Ahadian *et al*., 2018). In the past decades, organ-on-chips have been extensively applied to simulate the physiopathological environments of various organs, like heart (Marsano *et al*., 2016), teeth (França *et al*., 2020), kidney (Wilmer *et al*., 2016), intervertebral disc (Paillat *et al*., 2023; Salzer *et al*., 2023), and bone (Mansoorifar *et al*., 2021). However, microfluidic bone chips have not been extensively reported because natural bones are highly complex.

Generally, an organ-on-a-chip construct must follow the design principles based on a reductionist analysis of the targeted organ, i.e., capturing its physiological characteristics (Park *et al*., 2019). A specific extracellular matrix (ECM) could enhance organoid morphogenesis (Lancaster *et al*., 2013); for instance, the mineralization of the ECM is an essential and crucial process for physiological bone formation (Yang *et al*., 2023). In this paper, the microfluidic bone chip was designed based on data on trabecular separation from healthy and ovariectomy (OVX) animal models to mimic healthy and osteoporotic bone. To simulate the parameters of the bone microenvironment, the chip was created using soft lithography from polydimethylsiloxane (PDMS), whose Young's modulus (∼ 3 MPa) (Qi *et al*., 2021) is close to that of the bone ECM at the initial stage of bone formation (∼ 3.5 MPa) (Smith *et al*., 2016). Additionally, the inner surface was coated with type I collagen (the main component of bone ECM). Then, the directional microflows were provided by a micro pump to simulate the blood flow. Finally, an *in vitro* OP model utilizing the chip was established to evaluate possible mechanisms of pathological processes in OP (Fig. 1). Our results showed that a smaller microchannel (diameter is 200 μm) compared to a larger one (diameter is 350 μm) could significantly accelerate osteogenesis, which may be caused by cellular anisotropy. The increased expression of autophagy-related genes 7 (ATG7) indicated that autophagy was associated with alkaline phosphatase (ALP) activities, and the Hippo/YAP pathway may be involved in this process, which is in agreement with the findings of many prior pieces of research (Yang *et al*., 2023). This microfluidic bone chip would facilitate bone chip development, contribute to understanding bone pathology in OP, and exhibit its applicability in preclinical research.

Materials and Methods

Animals

Animal use was confirmed by the Ethics Committee at Sichuan University and performed under the China Council on Animal Care guidelines. Twelve C57BL/6 female mice were obtained from the GemPharmatech Co., Ltd (Changzhou, Jiangsu, China). (2-month-old). Mice were reared, as previously mentioned (Fang *et al*., 2022). In pathogen-free Conditions, 3 ~ 4 mice per cage were maintained at 25 °C with a 12 h light/dark period and ad libitum consumption of standard rodent diets and water.

OVX Mouse Model

The mice were randomized into the sham group (Sham, n = 6) and the OVX group (OVX, n = 6). As mentioned previously, all mice underwent sham surgery or bilateral ovariectomy one week after acclimatization (Inada *et al*., 2011). Mice were euthanized in week 12.

Micro-Computed Tomography

A Scanco vivaCT 80 (Scanco Medical AG, Brüttisellen, Switzerland) was utilized for micro-computed tomography (Micro-CT). X-ray sources at 70 kV and 114 μA were set, and the left femur's distal metaphysis excised was scanned. Each proximal region (~ 0.5 mm) was undertaken in the growth plate's most distal part. Based on three-dimensional (3D) digital imaging, we resolved parameters such as Tb.Sp (trabecular separation, μm).

Cell Culture

The Murine osteoblastic MC3T3-E1 cell line (catalog number: JNO-M0089) was procured from Guangzhou Jennio Biotech Co., Ltd. (Guangzhou, Guangdong, China). All cell lines were maintained at 37 ℃ in a 5 % (vol/vol) CO_2 incubator and were mycoplasma-free (CycleavePCR™ Mycoplasma Detection Kit, Beijing, China). We performed cell line authentication using the short tandem repeat (STR) analysis method and cross-checked the results with the International Cell Line Authentication Committee and the ExPASy Cellosaurus database to ensure that the cell lines were correctly identified.

MC3T3-E1 cells (MC3T3) were cultured with Dulbecco's modified eagle medium (DMEM, High Glucose, Gibco, Grand Island, NY, USA), supplemented with 10 % (vol/vol) fetal bovine serum (FBS., Cell-Box, HongKong, China) and 1 % (wt/vol) penicillin-streptomycin (Hyclone, Logan, UT, USA). The entire medium was replaced every 2 to 3 days. 10 mM β-glycerolphosphate disodium salt hydrate (Sigma-Aldrich, St. Louis, MO, USA), 10 nM dexamethasone (Sigma-Aldrich, St. Louis, MO, USA), and 50 μg/mL L-ascorbic acid (Sigma-Aldrich, St. Louis, MO, USA) were mixed into the entire DMEM medium for cell osteogenic differentiation. MC3T3-E1 cells were differentiated (pre-osteoblast to osteoblast) following the process until 7 days.

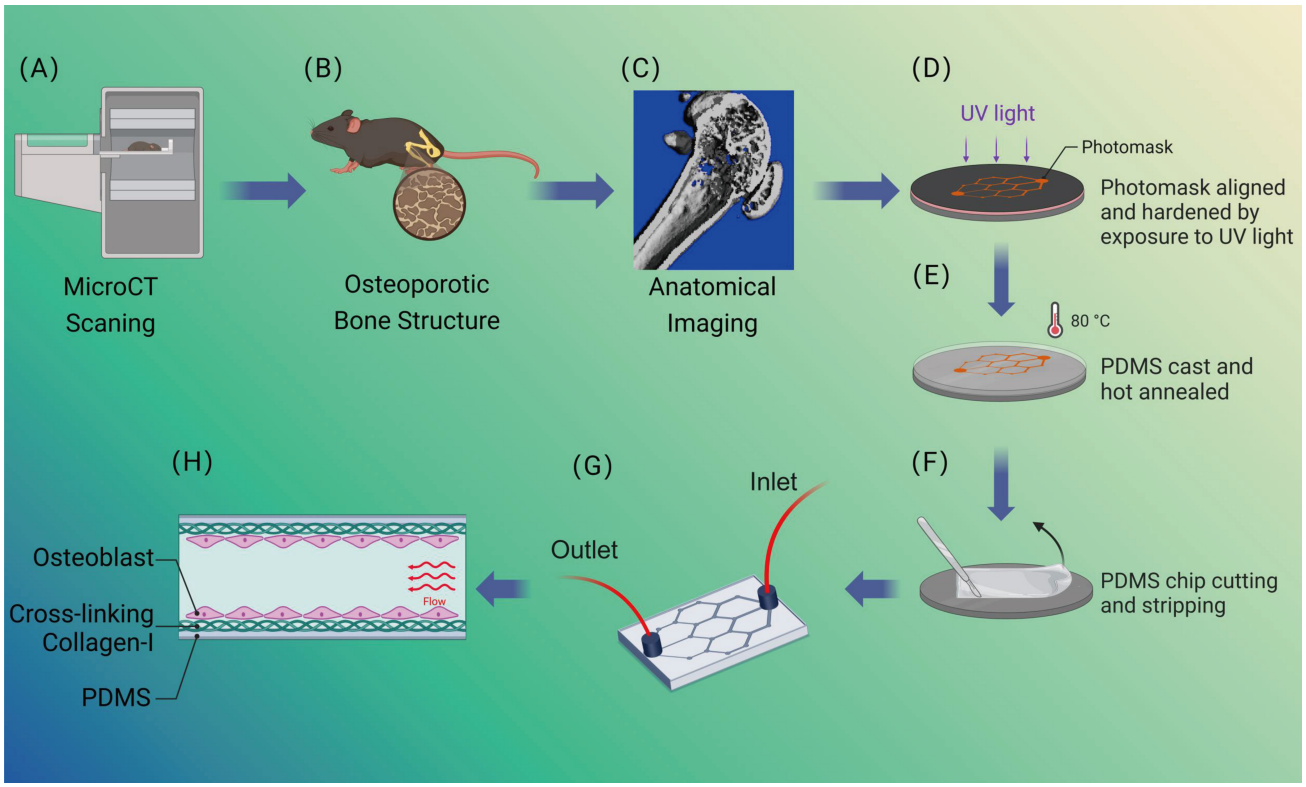

Fig. 1. Schematic diagram of the bone chip design and fabrication. (**A–C**) Illustration of the microfluidic bone chip on osteoporosis. MicroCT scanning (**A**) was used to obtain data from osteoporotic mice bone (**B**), and the parameters (**C**) were used for the chip microchannels design. (**D–F**) Brief diagram of the chip manufacturing process. Photomark aligned and hardened by exposure to UV light (**D**). PDMS cast and hot annealed (**E**). PDMS chip cutting and stripping (**F**). (**G**) Illustration of the microfluidic bone chip. (**H**) A side view of the microchannel components in the bone chip. Osteoblast cells are cultured on PDMS coated with collagen-I. PDMS, polydimethylsiloxane.

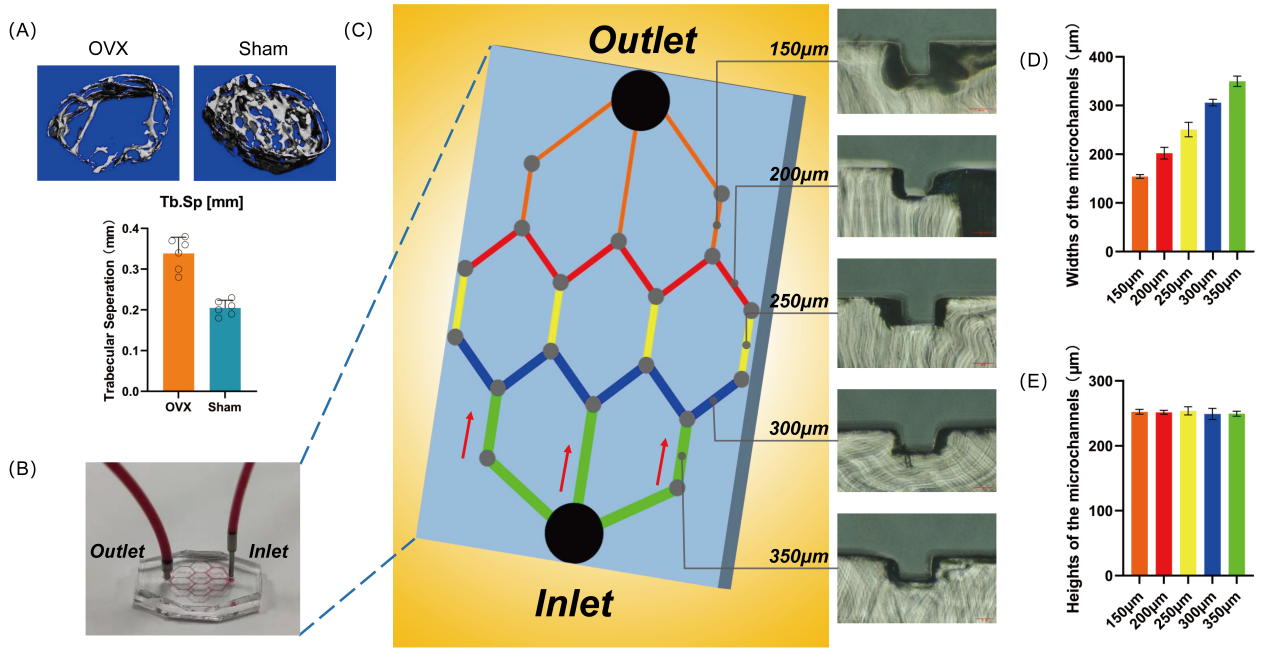

Fig. 2. Structure and characterization of the bone chip. (**A**) Data and images of the mean distance between trabeculae were assessed using MicroCT in both OVX and sham groups (n = 6). (**B**) Photograph of the bone chip. (**C**) Schematic of the bone chip. Measurement of width (**D**) and height (**E**) of microchannels. OVX, ovariectomy.

Cells were dissociated from a cell culture dish using trypsin-EDTA (biosharp, Beijing, China) for 1 min, then centrifuged at 1000 rpm for 5 min. The supernatant solution was removed, and the residual solution containing cells was mixed uniformly with the 6 mL new medium (DMEM with 10 % FBS) by blowing 10–20 times. Cell suspensions at a cell density of 5×10^5 cells/mL were seeded in the microchannels (Nelson *et al*., 2021). Cell density must be regulated once cells adhere to the microchannels to achieve density consistency for accurate further tests.

Cell Shape Analysis

The areas, perimeters, axial ratio, and orientation angles of ME3T3 cells were analyzed in the regions of interest (20 cells at least) obtained from images of cells in every microchannel using a microscope. Image J software v1.54f (National Institute of Health, Bethesda, MD, USA) calibrated the cellular area, perimeter, and axial ratio. The cell orientation angle is defined as the angle of the cell's long elliptical axis concerning the axis of the microchannel. The orientation angular distribution was analyzed by dividing them into groups of every 30° and counting the percentages.

Fabrication of the Bone Chip Based on Biomimetic Data

The microfluidic device was fabricated by PDMS (Polydimethylsiloxane, Dow Corning, Midland, WI, USA). Since PDMS is highly gas permeable, oxygen and carbon dioxide can be liberally exchanged across cell culture and the surrounding environment, facilitating real-time viewing and imaging. In addition, the fabricated chip can be sterilized by a UV zone. The chip consists of two PDMS layers. The upper layer with microchannels is reproduced from SU-8 photoresist microstructures fabricated via soft lithography, while the lower is flat. A 10:1 (w/w) mixture of PDMS prepolymer and curing agent was poured into a SU-8 mold and solidified overnight at 80 °C. Then, microchannels were manufactured after PDMS replicas peeled off the mold. Plasma oxidation, a routine bonding technique for PDMS, was utilized to combine the two layers (Pinto *et al*., 2017). The SU-8 photoresist was purchased from MicroChem (Suzhou, Jiangsu, China). The design and processing of the chip is presented in Fig. 1.

By simplifying the porous honeycomb structure of natural bones, an ideal combined serial and parallel microchannel connection structure was designed for this chip. The data of trabecular separation was used to create the width of microchannels in the chip, and the height of the microchannels is designed to be approximately 250 microns (due to the parameters of the SU-8 photoresist and the photolithography machine), which is sufficient to simulate the 3D structure of bones. Trabecular separation is one of the main parameters of bone trabeculae structure, which is the gap between the trabeculae and can be understood as porosity. After OVX mouse models were constructed, trabecular separation data of the OVX and sham groups were obtained by MicroCT, which was then used to design microchannel parameters in the chip to model porosity in healthy/osteoporotic bone.

To provide continuous nutrition to the cells, the inlet and outlet were created by punching holes in upper PDMS layers, and a micro-pump was used to provide a flowing culture medium. Inlet flow velocity was set at 100 µL/h. The loading fluid shear stress (FSS) was calculated according to the following formula as described previously (Su *et al*., 2021):

$$\tau = \frac{6\mu Q}{WH^2}$$

Where τ is the shear stress loaded to the cells; µ is the viscosity of the circulating medium; Q is the velocity of fluid; H is the height of the microchannel; and W is the width of the microchannel. Based on the parameters of the microchannels and the viscosity of the circulating medium (0.83×10^{-3} Pa · s), the shear stress was measured according to the velocity of the circulation medium. In this study, MC3T3 cells in each microchannel were exposed to stable laminar fluid shear stress for 24 h or 48 h immediately after 90 % confluency. The chip was kept in an incubator at 37 °C. The fluid may form a disturbed flow at the microchannel junction and harm cells. Therefore, we designed a buffer zone (gray zone, diameter is 500 µm) at each microchannel junction to reduce the adverse influence (Fig. 2**C**).

MC3T3 cells were seeded in microchannels. Before culturing cells, PDMS was autoclaved for 20 minutes at 121 °C. Immediately following autoclaving, the inner surface of the chip was coated with 1 mg/mL of Type I Collagen (Solarbio-China) solution premixed in phosphate-buffered saline (PBS) (Sigma-Aldrich, Saint Louise, Missouri, USA) at 4 °C for 4h to enhance cell adhesion on the chip surface. Ultimately, the extra Type I Collagen in the chip was wiped thoroughly 5 times with PBS. All other chemicals were obtained from Thermo Fisher Scientific (Waltham, Massachusetts, USA).

Antibodies and Immunofluorescent Staining

Our previous findings demonstrated that autophagy promotes osteogenesis in MC3T3 cells, and ATG7 is a vital marker protein for autophagy (Pei *et al*., 2022; Su *et al*., 2023). In this study, we used the autophagy inhibitor chloroquine (CQ) to determine the effect of autophagy on osteogenesis. Then, we investigated the expression levels of ATG7 and ALP. The primary antibodies for the immunofluorescence (IF) staining were mouse monoclonal anti-ATG7, rabbit polyclonal anti-ALP, and mouse monoclonal anti-YAP (yes-associated protein, YAP). The primary antibodies utilized are detailed in Table 1.

Firstly, the cells were immobilized with 4 % paraformaldehyde for 15 min under 4 °C. After 3 washes

Table 1. Detailed information on primary antibodies.

Antibody	Isotype	Manufacturer	Cat. No	Dilution (for IF)
ATG7	Mouse mAb	Proteintech (Wuhan, Hubei, China)	67341-1-Ig	1:200
ALP	Rabbit pAb	HuaBio (Hangzhou, Zhejiang, China)	ET1601-21	1:200
YAP	Mouse mAb	SAB (College Park, MD, USA)	48350	1:200

IF, immunofluorescence; ATG7, autophagy-related genes 7; ALP, alkaline phosphatase; YAP, yes-associated protein.

with PBS, 0.5 % Triton-100 was added. After 10 minutes, the cells were incubated in a PBS solution of 1 % BSA for 40 minutes. Subsequently, the primary antibodies of ATG7, ALP, and YAP were added into the samples and incubated till the next day under 4 °C, and fluorescent secondary antibodies were added next. The nucleus was stained by 2 mg/mL concentration 4',6-diamidino-2-phenylindole (DAPI) for 10 min. The positive cells were observed in a laser scanning confocal microscope (Zeiss, LSM710, Oberkochen, Baden-Württemberg, Germany). Immunofluorescence images were quantified by determining the mean fluorescence intensity (MFI) of cells in the chip viewed in three randomly chosen confocal images from biological independent samples using Image J (v1.54f). MFI values, calculated from the sum of the values of all the pixels in the region of interest divided by the number of pixels, are more likely to accurately reveal the shift in fluorescence intensity of a population of cells. Specific methods can be found in previous research publications (Shihan *et al*., 2020; Shihan *et al*., 2021). Cells cultured on PDMS substrates of the same material as the chip but without microchannels served as negative controls.

EdU Incorporation Assay

BeyoClick™ EdU Cell Proliferation Kit with Alexa Fluor 594 (Beyotime, Shanghai, China) was tested for cell proliferation in the chip. After 48 hours of cell culture, 50 μM of Edu solution was added to the chip. After continuing the incubation for 2 hours, cells were immobilized with 4 % paraformaldehyde at room temperature. After cleaning in PBS with 3 % bovine serum albumin (BSA, Biosharp, Hefei, Anhui, China) 3 times, cells were cultivated with 1 × Apollo solution for 30 min at room temperature, avoiding the light. Finally, cells underwent nuclear staining with 1 × Hoechst for 30 min and then viewed by fluorescence microscopy. Here, slide-cultured cells were used as a negative control because most of the conclusions of past studies about EdU assays came from this traditional 2D cell culture method.

CCK-8 Assay

Cell viability was analyzed by Cell Counting Kit-8 (CCK8, Beyotime, Shanghai, China) according to the manufacturer's protocols. After cultured in the chip for 24 hours, cells of equal seeding area were collected from each group and placed in 96-well microplates (Corning, NY, USA). Specifically, take the 200 μm microchannel as an example; the surface area of a single well in 96-well microplates is approximately 0.3 cm^2, equal to the total area of 15 cm length of microchannel. The desired microchannel parts in the chip are cut out using a scalpel and collected. The cells therein were digested with trypsin and placed in a single well of a 96-well microplate. Then, 10 μL of CCK-8 reagent was added to each well and cultured at 37 °C for 2 hours. All experiments were performed in triplicate. The absorbance was determined at 450 nm by microplate reader (BioTek, Winooski, Vermont, USA). Finally, the cell viability rate was expressed as a ratio (%) between the absorbance of the treated group and that of the control group.

ALP Activity Assay

The ALP activity was evaluated quantitatively using commercially available kits. The ALP activity in lysate was evaluated colorimetrically with the Alkaline Phosphatase Assay Kit (Beyotime, Shanghai, China), which was based on the conversion of colorless p-nitrophenyl phosphate (pNPP) to colored p-nitrophenol after co-incubation for 15 min at 37 °C. The results were normalized to the total intracellular protein content determined by the bicinchoninic acid (BCA) Protein Assay Kit (Beyotime, Shanghai, China) and expressed in nanomoles of produced p-nitrophenol per min per mg of protein (nmol/min/mg protein).

Statistical Analysis

Each experiment was tested on three devices, and three individual results were performed to obtain data. All statistics were assessed using either a two-tailed Student's *t*-test or one-way ANOVA with Tukey's post hoc test performed using GraphPad Prism 9.0.0 software (GraphPad Software Inc., San Diego, CA, USA). Data were indicated as mean ± SD, and statistical significance was expressed as $*p < 0.05$, $**p < 0.01$, $***p < 0.001$, and $****p < 0.0001$.

Results

Identification and Characterization of the Chip

The OVX mouse model was first successfully constructed and characterized, and the relevant data are presented in the Supplementary Information (**Supplementary Fig. 1**).

As shown in Fig. 2**A**, the trabecular separation result in the OVX group was (0.338 ± 0.040) mm compared to (0.205 ± 0.019) mm in the sham group. Considering

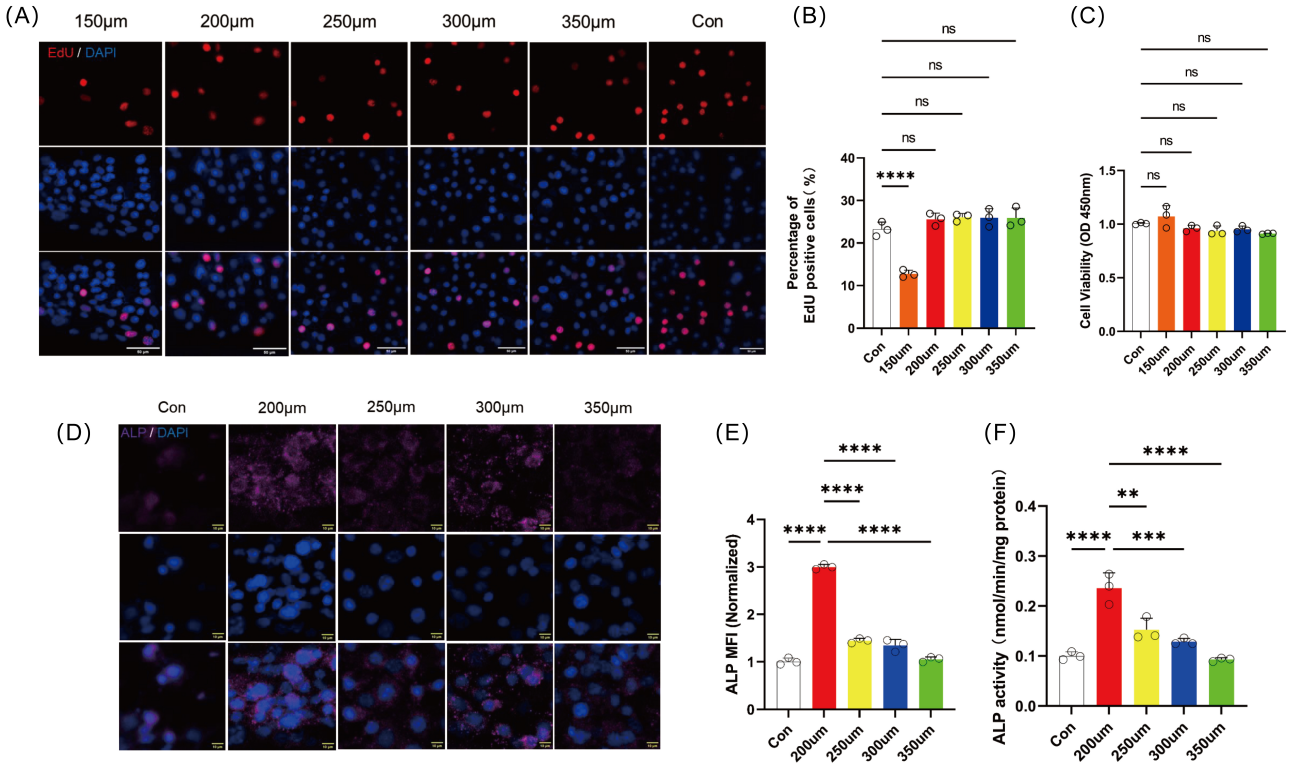

Fig. 3. Biological evaluation of the bone chip. (**A**) EdU staining was used to evaluate the proliferation of MC3T3 cells. The regeneration cells were stained by EdU assay (red). The nuclei were stained by DAPI (blue). Scale bar = 50 μm (EdU stain). (**B**) Statistical analysis of percentages of Edu-positive cells obtained from (**A**). (**C**) CCK-8 assay was used to evaluate cell viability in all microchannels after 24 hrs. (**D**) The osteogenic capability of MC3T3 cells cultured in 200 μm–350 μm microchannels after 48 hrs using IF staining: ALP (magenta) and DAPI (blue). Scale bar = 10 μm. (**E**) Normalized MFI of ALP. (**F**) ALP activity of cells cultured in 200 μm–350 μm microchannels after 24 hrs. Data are shown as the means ± SD. $^{**}p < 0.01$, $^{***}p < 0.001$, $^{****}p < 0.0001$. ns, not significant. DAPI, 4',6-diamidino-2-phenylindole; MC3T3, MC3T3-E1 cells; ALP, alkaline phosphatase; MFI, mean fluorescence intensity.

that pore size changes in natural bone are a continuous spatiotemporal process, a range of microchannel widths from 150 μm to 350 μm (50 μm intervals) was designed to reproduce the structural characteristics of healthy and OP bone, and the changing spatiotemporal processes between them. The microchannels were integrated into a single chip to minimize experimental errors.

Five different widths of microchannels were fabricated as a series-parallel structure (Fig. 2**B**) to mimic the porous honeycomb structure of natural bone (150 μm, orange; 200 μm, red; 250 μm, yellow; 300 μm, blue; and 350 μm, green). The black zones are the inlet and outlet (1500 μm in diameter) and were designed to be large enough to allow smooth microfluidic inflow and outflow. The grey zones are connections between microchannels used to avoid damage to cells by bending corners. The red arrows indicate the direction of microfluid flow. The culture medium was pumped in from the side of the 350 μm microchannel and out through the 150 μm microchannel side, which was designed to simulate the direction of blood flow from cancellous bone to compact bone in natural bone (Fig. 2**C**).

As shown in Fig. 2**D, E**, the width of the chip is (154.3 ± 3.9) μm, (202.2 ± 12) μm, (250.8 ± 14.8) μm, (306 ± 6.9) μm, (349.8 ± 10.6) μm, and the height is (252.5 ± 3.7) μm, (251.7 ± 3) μm, (253.9 ± 6.3) μm, (249.1 ± 8.6) μm, (249.6 ± 3.8) μm. These results indicate that the chip constructed a 3D structure that met the design requirements and simulated healthy/OP trabecular separation.

Next, we calculated the FSS on cells in each microchannel of the chip that uses such a combined serial and parallel microchannel connection structure. As shown in Fig. 2**C**, there are three 350 μm microchannels in each chip with a total width of about 1050 μm, in which the cells were exposed to FSS of 0.023 dym/cm^2. The FSS calculated for the other groups by this method was 0.011 dym/cm^2 (300 μm), 0.020 dym/cm^2 (250 μm),0.017 dym/cm^2 (200 μm),0.044 dym/cm^2 (150 μm), respectively. These results show that the cells in each microchannel are exposed to very weak FSS only, suggesting that the microfluidics in this chip do not have any mechanical effect on the cells other than providing nutrients.

Assessment of in-Chip Cell Proliferation and ALP Activity on MC3T3 Cells

The proliferation of MC3T3 cells in each microchannel was tested using an EdU stain (Fig. 3**A**). The results

(Fig. 3**B**) showed that the EdU positive cells ratio in the 150 µm microchannel was significantly lower than in the control group ($p < 0.0001$). In contrast, the EdU positive cells ratio in 200 µm ~ 350 µm microchannels was not substantially different from the control group. The results of the CCK-8 assay (Fig. 3**C**) showed no significant difference in cell viability in each microchannel. Due to the affected cell proliferation in the 150 µm microchannels, we removed this subgroup in the following study.

Next, by laser confocal microscopy, ALP level was detected in 200 µm ~ 350 µm microchannels by IF staining (Fig. 3**D**). ALP is an essential biomarker in cellular osteogenesis, which can promote the formation of mineralized active bone (Vimalraj, 2020). As shown in Fig. 3**C**, the magenta fluorescent signal of ALP in the 200 µm microchannel was more visible and substantial than in other groups after 48 hrs cultured. The MFI of ALP (Fig. 3**E**) in the 200 µm microchannel was higher than others. At the same time, the MFI of ALP in the 350 µm microchannel was significantly lower than others. The results of the ALP activity assay also showed that the cells in the 200 µm microchannels had the strongest enzyme activity while the cells in the 350 µm microchannels were weakest (Fig. 3**F**). The above results showed that the cellular osteogenic capacity was strongest in 200 µm microchannel while the weakest was in 350 µm microchannel. Negative staining controls of fluorescent secondary antibodies without background staining in all groups were shown in (**Supplementary Fig. 3**).

Cell Anisotropy and Morphology Changes in Each Microchannel

We then analyzed the cytological behavior in each group, hoping to find some clues to explain the differences above. We first defined the cell orientation angle (Fig. 4**A**), i.e., the angle between the cell ellipse's long axis and the microchannel's long axis (less than 90°). Representative light microscopic images of the cells in 200 µm ~ 350 µm microchannels are shown in Fig. 4**B–E**. The cell area (Fig. 4**F**) and perimeter (Fig. 4**G**) in the 200 µm microchannels differed significantly from those in other microchannels. Still, the axial ratio (Fig. 4**H**) of cells in the different microchannels did not vary significantly. It prompts us that the cells in the 200 µm microchannels may be compressed proportionally, leading to some physiological changes in cell function.

The cell orientation angle (Fig. 4**I**) in the 200 µm microchannels was significantly different from that in the 300 µm and 350 µm microchannels but not from that in the 250 µm microchannels. Interestingly, the cell orientation angle in 250 µm microchannels was not significantly different from that in 300 µm and 350 µm microchannels, and this may indicate that the 250 µm microchannel could be a transitory stage between 200 µm microchannel and 300/350 µm microchannel. In conclusion, the cell orientation angle in the 200 µm microchannel differs from the others.

Then, the cytological changes in the 200 µm microchannel were focussed on. It is shown that 80 % of the cells in the 200 µm microchannel were clustered in the range of 0 ~ 30°, a rate that greatly exceeded that in the other three groups (55 %, 30 %, 20 %) (Fig. 4**J–M**). It makes the cells in the 200 µm microchannel aligned along the microchannel more obviously. Combined with the above results, we can hypothesize that the more robust osteogenic capacity of cells in the 200 µm microchannel may be correlated to their unusual anisotropy.

Inhibition of Autophagy Reduces Cellular Osteogenesis

As shown in Fig. 5**A**, the red fluorescent signal of ATG7 in every microchannel was more visible after CQ was used, while the green fluorescent signal of ALP was less evident than before. The MFI of increased-ATG7 (Fig. 5**B–F**) and decreased-ALP (Fig. 5**G–K**) were statistically significant in all groups. On the other hand, The MFI of ALP in each microchannel was reduced after CQ was used, which confirms the positive correlation between autophagy and osteogenesis.

The same assays were performed after reversing the direction of the microfluidics to verify the scientific nature of the chip. As shown in **Supplementary Fig. 2**, the results and trends were the same as the previous results. It indicates that the physiological behaviors of the cells in each microchannel are independent of each other, and the series structure of the chip did not lead them to affect each other.

YAP is Involved in Osteogenetic Differences in Different Microchannels

Mounting evidence suggests that YAP is crucial in the formation and remodeling of bone (Pan *et al*., 2018). Here, we focus on the expression levels of YAP in 200 and 350 µm microchannels to investigate the potential molecular mechanisms behind them. As shown in Fig. 6**A**, the red fluorescent signal of YAP in the 200 µm microchannel was more visible than in the 350 µm microchannel. The MFI of YAP (Fig. 6**B**) was statistically significant between the two microchannels. In addition, we analyzed the nuclear translocation of YAP. We found that the nuclear translocation of YAP was more evident in the 200 µm microchannel (Fig. 6**C**), which prompts the involvement of YAP in cellular activities and may influence cytological behavior. The grey values of the radial distribution of YAP in the nucleus also differed in the 200 µm and 350 µm microchannels (Fig. 6**C–E**).

Discussion

Bone formation is the process by which mineralization accumulates in large pores (2D sectional drawing of large microchannels) and gradually forms small pores (2D sectional illustration of small microchannels). Osteoporosis might result from decreased osteogenic capacity, which leads to abnormal mineral deposition in large microchan-

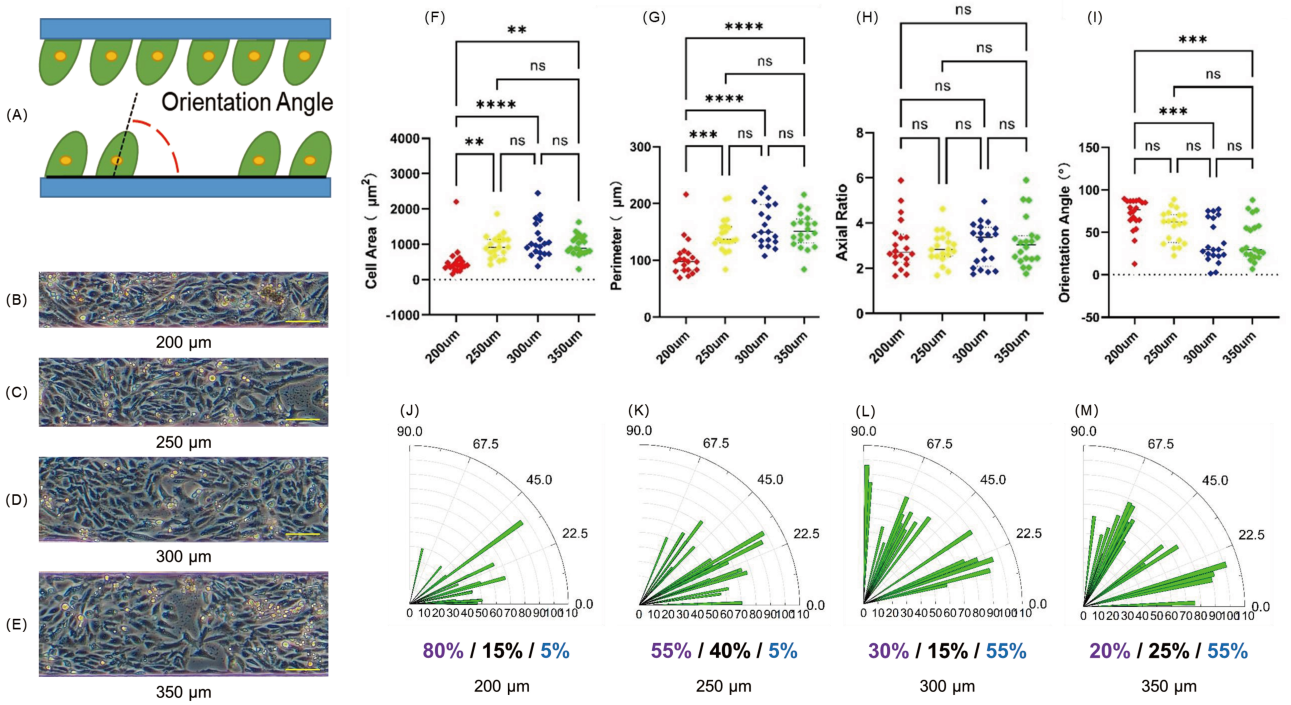

Fig. 4. MC3T3 cells cultured in the chips showed different anisotropic behavior. (**A**) Diagram of cell orientation angle. (**B–E**) Light microscope images in 200 μm ~ 350 μm microchannels. Scale bar = 100 μm. Comparison of cell area (**F**), perimeter (**G**), axial ratio (**H**), and orientation angle (**I**) of MC3T3 cells cultured in 200 μm ~ 350 μm microchannels. $^{**}p < 0.01$, $^{***}p < 0.05$, $^{****}p < 0.0001$. ns, not significant. (**J–M**) Proportion and distribution of orientation angles in 200 μm ~ 350 μm microchannels: 0° ~ 30°, purple; 30° ~ 60°, black; 60° ~ 90°, blue.

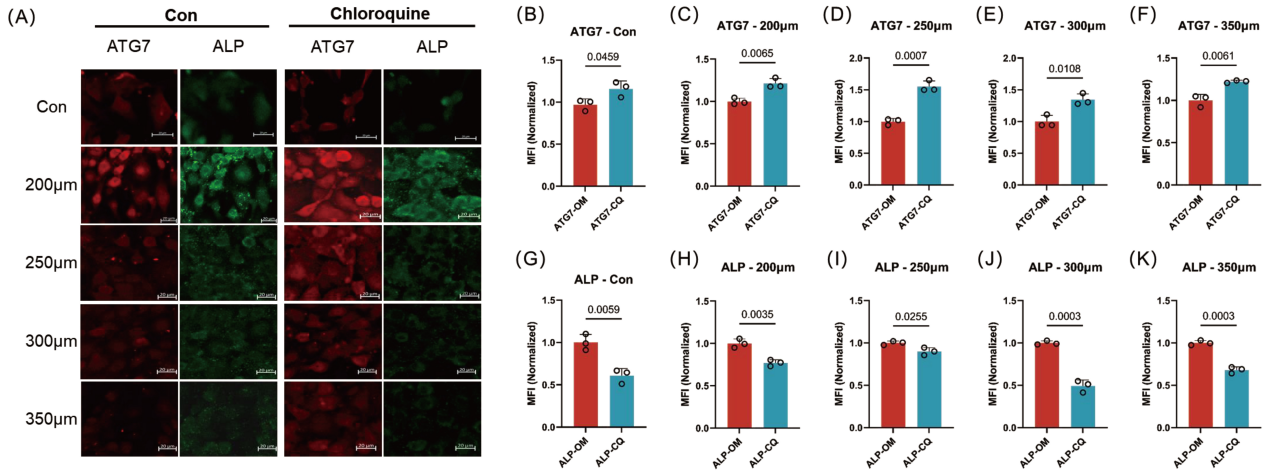

Fig. 5. Chloroquine (CQ) inhibited the osteogenic ability of MC3T3 cells. (**A**) IF staining of MC3T3 cells cultured in 200 μm ~ 350 μm microchannels with/without CQ used: ATG7 (red) and ALP (green). Scale bar = 20 μm. Normalized MFI of ATG7 (**B–F**) and ALP (**G–K**) protein expression obtained from (A). ATG7, autophagy-related genes 7.

nels and an inability to form small microchannels, resulting in a loose, porous structure. The design of biomimetic devices to mimic the diverse physicochemical properties of bone ECM has received particular attention (Curry *et al*., 2016; Freeman *et al*., 2019; Remmers *et al*., 2020). These biomimetic features are crucial for bone formation and function. The architecture of the bone chip should be based on the design principle of reductive analysis, and the first step is to seize the anatomical features of the bone and reduce them to the essential elements necessary for physiological function. Therefore, in the present study, we investigated a crucial element, trabeculae separation, in healthy and osteoporotic bone tissues and accurately reproduced it using soft lithography. The present chip constructed using

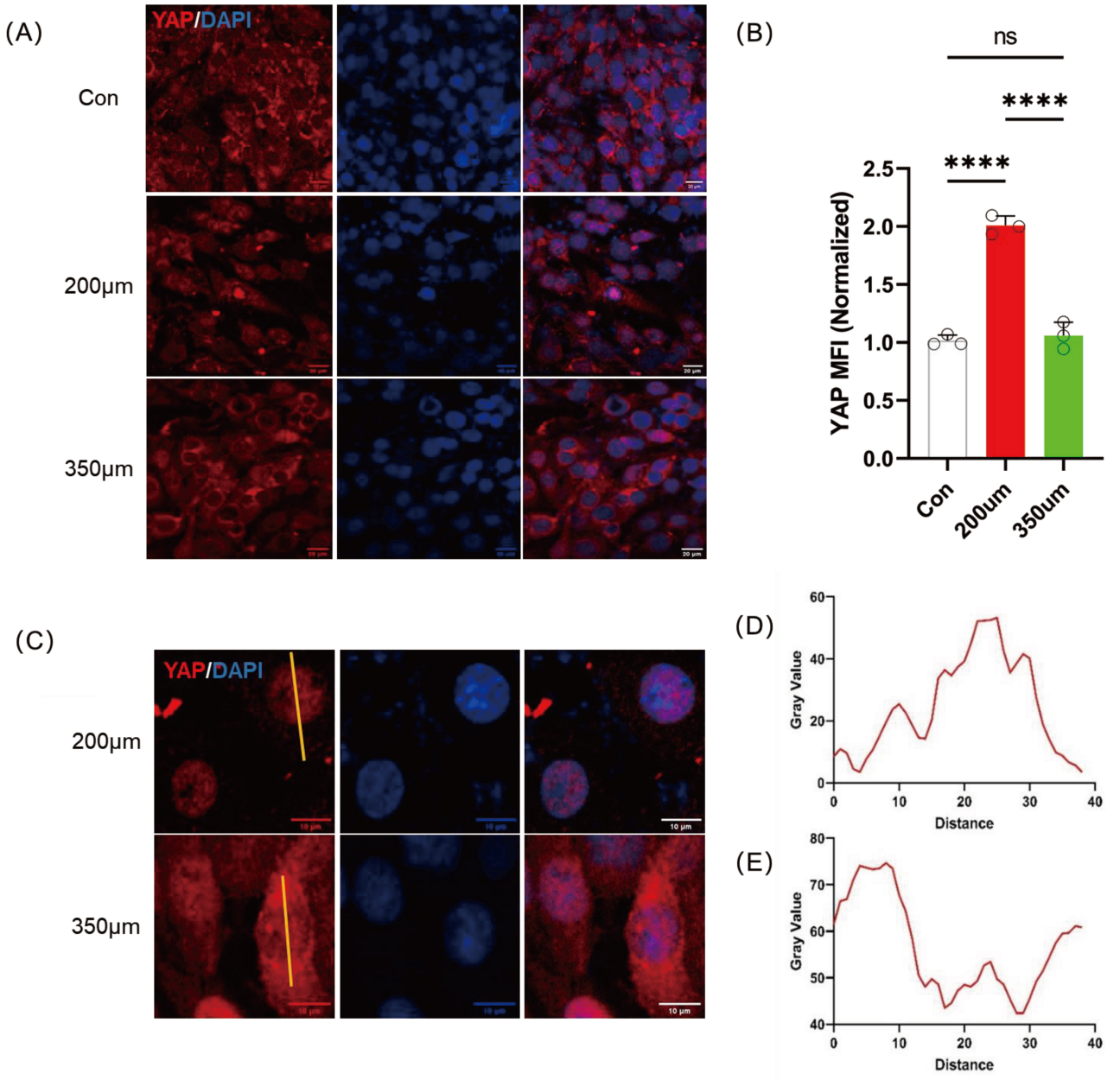

Fig. 6. MC3T3 cells cultured in 200 μm microchannels showed higher YAP expression and induced translocation of YAP into the nucleus. (**A**) IF staining of MC3T3 cells cultured in 200 μm and 350 μm microchannels for 48 hrs: YAP (red) and DAPI (blue). Scale bar = 50 μm. Normalized MFI of YAP (**B**) obtained from (**A**). ****$p < 0.0001$. ns, not significant. (**C**) Representative image of YAP nuclear translocation in 200 μm and 350 μm microchannels: YAP (red) and DAPI (blue). Scale bar = 10 μm. The radial distribution of YAP (yellow line) in the cell nucleus staining intensity (gray value) in 200 μm (**D**) and 350 μm (**E**) microchannels. YAP, yes-associated protein; IF, immunofluorescence.

data on trabeculae separation from the metaphyseal bone may be beneficial for studying the mechanisms underlying the healing processes of metaphyseal bone fractures (Alagboso *et al*., 2019). Generally, healthy and osteoporotic bone co-exist in OP patients. Therefore, the microchannel widths were set from 150 μm to 350 μm and integrated into a single chip to simulate the spatiotemporal changes of trabecular separation during the pathological process of natural bone from healthy to OP. Another advantage of integrating microchannel widths in a single chip is that experimental error can be reduced. To make the cell culture substrate components as similar as possible to the ECM, the upper and lower layers of the chip are made of PDMS (matrix stiffness close to ECM), and the inner surface of the chip is coated with type I collagen (the main component of ECM), which better reproduces the physiological properties of ECM. In addition, we used micro pumps to provide microfluidics for a continuous supply of nutrients to the cells but without in-

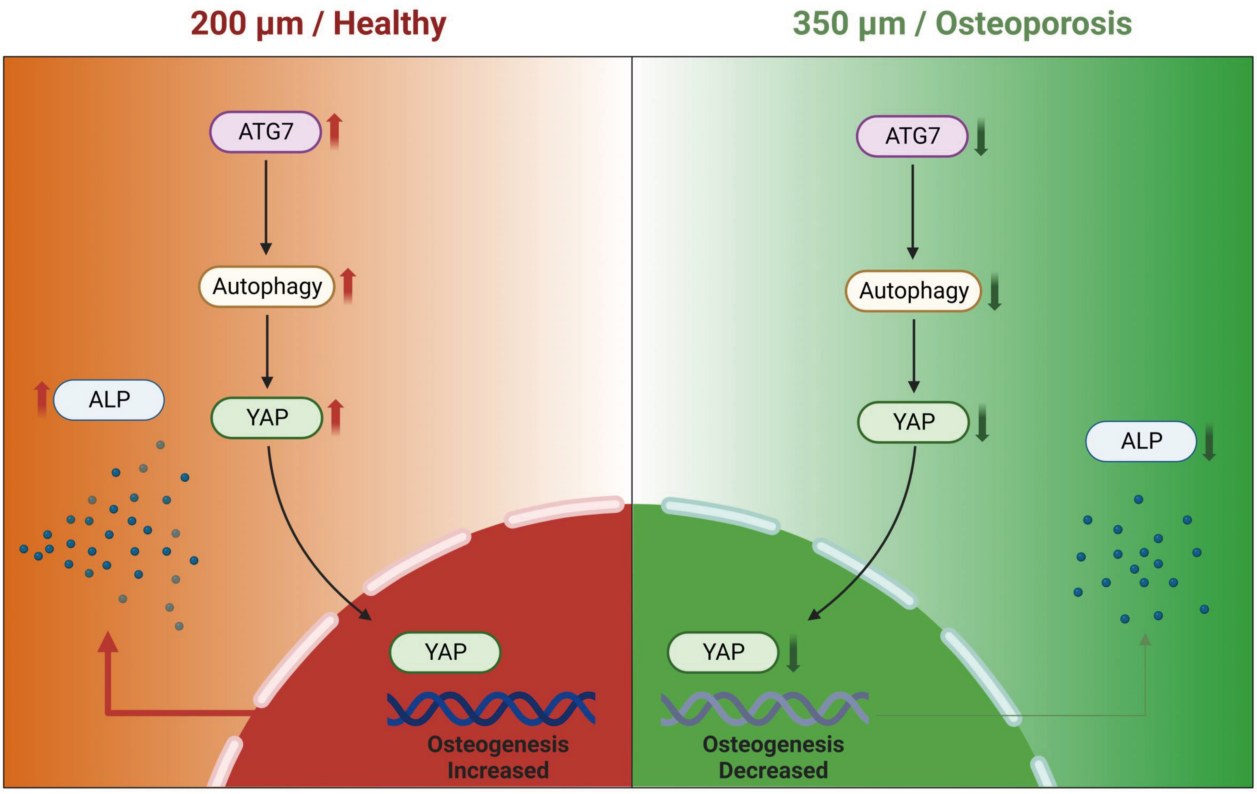

Fig. 7. Schematic diagram of osteogenesis in the bone chip on osteoporosis.

creasing the effect of FSS. In summary, we attempted to fabricate a biomimetic chip with some bone microenvironmental features.

As shown in Fig. 3, the cells in the 200 µm microchannel (mimicking the trabecular separation of healthy mice) demonstrated a stronger osteogenic capacity than other groups, while the cells in the 350 µm microchannel (mimicking the trabecular separation of OVX mice) had the weakest osteogenic capacity. These results suggest that the diameter size of the microchannels may be an essential cause of the differences in osteogenic capacity. These results might help design biointerfaces for implants used for osteoporosis and develop platforms for testing osteoporosis drugs. However, due to the limitations of soft lithography, the cross-section of the microchannels in the chip is rectangular rather than elliptical as in the natural bone, which may have some adverse effects on the cells. In addition, this study did not detect the role of FSS, an important osteogenesis-promoting factor. We will conduct further research on these issues in the future.

Anisotropy is an omnipresent feature of the cellular environment (Le Saux *et al*., 2020). Variations in the ECM composition and how its organized components lead to considerably different topographies, each suited for the functional needs of the related tissues (Reddi *et al*., 1977). A strong relevance exists between the anisotropy of the cell environments and cellular functions (Théry *et al*., 2006). Thus, anisotropy can influence cell behavior (Wang *et al*., 2020), including osteogenesis (Chen *et al*., 2022). Therefore, in this study, we isolated the microchannel scale as a variable to detect anisotropy. If anisotropy is shown to depend on varied microchannel scales, anisotropy induced by the pore scale is established as a sufficient factor (not necessarily the only factor). In the present study, cells in 200 µm microchannel showed unusual anisotropy, corresponding to the highest levels of ALP expression. It suggests that anisotropy may lead to changes in cell function, for example, promoting osteogenesis. In addition, the cell area and perimeter in the 200 µm microchannel were also significantly lower than that in the other groups, but the axial ratio did not change significantly. We can hypothesize that the narrower channel compressed these cells and eventually promoted their osteogenesis. This hypothesis may involve studies related to cell-volume-control mechanisms, which we did not investigate in this study. We will explore this work in the future. Overall, we highlight that microchannels with different scales in the chip mimic the physiological differences between healthy and OP bone and facilitate osteogenesis through anisotropy.

Autophagy is a hyper-regulated procedure that involves the turnover of cytoplasmic contents, long-lived proteins, or impaired cellular organelles. Bone remodeling depends on proteostasis, while dysfunctional proteostasis during aging can fail to sustain bone homeostasis (Ma *et al*., 2023). Autophagy dysregulation is relevant to numerous aging and degenerative diseases, such as Parkinson's

disease, Alzheimer's disease, and osteoporosis (Li *et al*., 2019a). Previous evidence showed that autophagy is a crucial bone homeostasis regulator, suggesting a novel therapeutic strategy for bone loss (Li *et al*., 2018). In addition, autophagy plays a vital role in osteoporosis caused by OVX and aging-induced bone loss (Ma *et al*., 2018). Since osteoblasts are in charge of ECM synthesis and are subsequently mineralized, autophagy in osteoblasts is thus expected to perform a critical role in bone formation (Hocking *et al*., 2012). Our team's previous studies have shown that autophagy regulates osteogenesis in MC3T3-E1 cells, so we chose MC3T3-E1 cells as the research object. ATG7 (Mizushima and Komatsu, 2011) is one multifaceted core protein that drives the cardinal stages of classical degradative autophagy through ATG8 lipidation (Collier *et al*., 2021). Evidence suggests that Atg7 deficiency in osteocytes inhibits autophagy, leading to bone loss (Onal *et al*., 2013). In this study, the highest levels of ATG7 were found in 200 μm microchannels, whereas the lowest levels of ATG7 were found in 350 μm microchannels. It suggests that autophagy was participating in the physiological activities involved. Unexpectedly, ATG7 increased after autophagy inhibitor CQ was used. The possible reason is that during autolysosome formation, CQ can increase the lysosomal pH and prevent autophagy-lysosome degradation (García-Prat *et al*., 2016). That may have led to an ATG7 increase and accumulation in the early stages of autophagy (Collier *et al*., 2021). It again demonstrated that autophagy was involved in physiological behaviors in each microchannel. Meanwhile, ALP levels were highest in 200 μm microchannels and lowest in 350 μm microchannels. The results of the ALP activity assay showed a similar trend. CQ decreased ALP levels in all microchannels, validating the relationship between autophagy and osteogenesis. The above results suggest that as individual factors, 200 μm and 350 μm microchannels can lead to similar osteogenic differences in healthy and OP bone. Due to the cell culture time duration of only 48 hours, we chose only ATG7 and ALP to validate biological differences in the early stages of osteogenesis. While other research assays (e.g., WB, qt-PCR) could better study the differences in cell populations within the chip, they would require pooling cells from multiple devices to gain enough cells for a robust assay. We believe that the images and results presented here could demonstrate the usefulness of this microfluidic chip, which could provide critical insights into the early stages of osteogenesis. It is essential to underscore that the purpose of this chip was not to detect the final differences in biomineralization in each microchannel but rather to study the impact of 3D morphology (mimics the structural features of healthy/OP bone) on osteogenesis and to better understand the osteoblast physiological differences in more *in vivo* like conditions – as such we did not optimize the conditions to maximize the culture time and osteoblast proliferation.

The Hippo/YAP signaling pathway can modulate the growth of organs and cells in development and regeneration (Moya and Halder, 2019). As the main component of the Hippo pathway, YAP travels between the plasm and nucleus of the cell. In the nucleus, YAP acts with the transcription factor TEAD to facilitate the expression of various growth-associated genes (Zhao *et al*., 2008). Our independent laboratory has been studying the effect of YAP on response to mechanical cues from biomaterials and extracellular stimuli to modulate various cellular behaviors, which provided some thought for this study (Yu *et al*., 2021; Yu *et al*., 2022a; Yu *et al*., 2022b). YAP is involved in osteogenesis through different biological mechanisms (Zhou *et al*., 2020; Zhu *et al*., 2023), and its absence in osteoblasts reduces bone mass (Xiong *et al*., 2018). YAP-CKO mice also have reduced bone mass (Kegelman *et al*., 2018), and YAP inactivation reduces bone formation defects in MC3T3 cells (Pan *et al*., 2018). YAP increases the transcription and function of the bone morphogenetic protein (BMP) (Alarcón *et al*., 2009), which is essential for bone. As YAP nuclear localization is associated with osteogenesis (Dupont *et al*., 2011), we investigated the correlation between YAP nuclear translocation and osteogenesis in different groups. The results showed that the MFI of YAP in 200 μm microchannels (especially in the nucleus) was significantly higher than that of YAP in 350 μm microchannels and was consistent with ALP and autophagy levels. These results suggest that the YAP-autophagy axis promotes osteogenesis in MC3T3 cells, aligning with some prior research conclusions (Li *et al*., 2019b). Further investigation of YAP-related upstream and downstream signaling pathway changes and their relationship with autophagy and osteogenesis may help to explain differences in osteogenic outcomes in the OP/healthy bone microenvironment.

Conclusions

In the present study, a bioinspired bone chip was developed using microfluidic technology. It validated the osteogenetic effects of the YAP-autophagy axis in 200/350 μm microchannels that mimic healthy and osteoporotic bone (Fig. 7). The bone chip has integrated physiological features of bone structure for bone formation. The idea behind the chip's design, which uses individualized anatomic data and certain cells to test for specific tissue diseases, can be applied to preclinical human studies, even though it derived its data from mice in this study. This bone chip may have positive implications for osteoporotic bone research, providing significant, predictive, and supplementary outcomes for in vivo and *in vitro* observations. Hence, this new bone chip will contribute to understanding the bone formation process in OP, enlightening novel mechanisms behind osteoporosis and bone loss-related diseases and opening new thoughts of developing biomaterials and therapeutics for OP.

List of Abbreviations

PDMS, polydimethylsiloxane; CQ, chloroquine; OP, osteoporosis; ECM, extracellular matrix; OVX, ovariectomy; ATG7, autophagy-related genes 7; ALP, alkaline phosphatase; Micro-CT, micro-computed tomography; 3D, three-dimensional; MC3T3, MC3T3-E1 cells; PBS, phosphate-buffered saline; IF, immunofluorescence; YAP, yes-associated protein; DAPI, 4',6-diamidino-2-phenylindole; MFI, mean fluorescence intensity; pNPP, p-nitrophenyl phosphate; BCA, bicinchoninic acid; BMP, bone morphogenetic protein; BSA, bovine serum albumin; CCK8, cell counting kit-8; DMEM, Dulbecco's modified Eagle medium; FBS, foetal bovine serum; FSS, fluid shear stress; STR, short tandem repeat.

Availability of Data and Materials

The datasets used and/or analyzed are available from the corresponding author on reasonable request.

Author Contributions

JY and XL conceptualized the study and designed the experiments. JY conducted the experiments. JY, PD, QL, FF, and HY performed data analysis and visualization. XL critically revised the manuscript. All authors contributed to editorial changes in the manuscript, read and approved the final manuscript, and have participated sufficiently in the work to take public responsibility for appropriate portions of the content. All authors have agreed to be accountable for all aspects of the work.

Ethics Approval and Consent to Participate

The Ethics Committee at Sichuan University confirmed the study (Ethics Approval number: K2021015).

Acknowledgments

The authors would like to thank Dr. Li Chen from Analytical & Testing Center, Sichuan University for her help with micro-CT scanning.

Funding

This study was supported by the National Natural Science Foundation of China (Grant numbers 11932014, 12372315, and 31971239) and Sichuan Science and Technology Program (Grant numbers 2022NSFSC0765 and 2022ZYD0079).

Conflict of Interest

The authors declare no conflict of interest.

Supplementary Material

Supplementary material associated with this article can be found, in the online version, at https://doi.org/10.22203/eCM.v047a15.

References

Ahadian S, Civitarese R, Bannerman D, Mohammadi MH, Lu R, Wang E, Davenport-Huyer L, Lai B, Zhang B, Zhao Y, Mandla S, Korolj A, Radisic M (2018) Organ-On-A-Chip Platforms: A Convergence of Advanced Materials, Cells, and Microscale Technologies. Advanced Healthcare Materials 7: 10.1002/adhm.201700506. DOI: 10.1002/adhm.201700506.

Alagboso FI, Budak M, Sommer U, Ray S, Kaiser A, Kampschulte M, Henss A, Dürselen L, Biehl C, Lips KS, Heiss C, Thormann U, Alt V (2019) Establishment of a clinically relevant large animal model to assess the healing of metaphyseal bone. European Cells & Materials 37: 444-466. DOI: 10.22203/eCM.v037a27.

Alarcón C, Zaromytidou AI, Xi Q, Gao S, Yu J, Fujisawa S, Barlas A, Miller AN, Manova-Todorova K, Macias MJ, Sapkota G, Pan D, Massagué J (2009) Nuclear CDKs drive Smad transcriptional activation and turnover in BMP and TGF-beta pathways. Cell 139: 757-769. DOI: 10.1016/j.cell.2009.09.035.

Chen J, Chen J, Zhu Z, Sun T, Liu M, Lu L, Zhou C, Luo B (2022) Drug-Loaded and Anisotropic Wood-Derived Hydrogel Periosteum with Super Antibacterial, Anti-Inflammatory, and Osteogenic Activities. ACS Applied Materials & Interfaces 14: 50485-50498. DOI: 10.1021/acsami.2c12147.

Collier JJ, Suomi F, Oláhová M, McWilliams TG, Taylor RW (2021) Emerging roles of ATG7 in human health and disease. EMBO Molecular Medicine 13: e14824. DOI: 10.15252/emmm.202114824.

Compston JE, McClung MR, Leslie WD (2019) Osteoporosis. Lancet (London, England) 393: 364-376. DOI: 10.1016/S0140-6736(18)32112-3.

Curry AS, Pensa NW, Barlow AM, Bellis SL (2016) Taking cues from the extracellular matrix to design bone-mimetic regenerative scaffolds. Matrix Biology: Journal of the International Society for Matrix Biology 52-54: 397-412. DOI: 10.1016/j.matbio.2016.02.011.

Dupont S, Morsut L, Aragona M, Enzo E, Giulitti S, Cordenonsi M, Zanconato F, Le Digabel J, Forcato M, Bicciato S, Elvassore N, Piccolo S (2011) Role of YAP/TAZ in mechanotransduction. Nature 474: 179-183. DOI: 10.1038/nature10137.

Ensrud KE, Crandall CJ (2017) Osteoporosis. Annals of Internal Medicine 167: ITC17-ITC32. DOI: 10.7326/AITC201708010.

Fang F, Ni Y, Yu H, Yin H, Yang F, Li C, Sun D, Pei T, Ma J, Deng L, Zhang H, Wang G, Li S, Shen Y, Liu X (2022) Inflammatory endothelium-targeted and cathepsin responsive nanoparticles are effective against atherosclerosis. Theranostics 12: 4200-4220. DOI: 10.7150/thno.70896.

França CM, Tahayeri A, Rodrigues NS, Ferdosian S, Puppin Rontani RM, Sereda G, Ferracane JL, Bertassoni LE (2020) The tooth on-a-chip: a microphysiologic

model system mimicking the biologic interface of the tooth with biomaterials. Lab on a Chip 20: 405-413. DOI: 10.1039/c9lc00915a.

Freeman FE, Browe DC, Nulty J, Von Euw S, Grayson WL, Kelly DJ (2019) Biofabrication of multiscale bone extracellular matrix scaffolds for bone tissue engineering. European Cells & Materials 38: 168-187. DOI: 10.22203/eCM.v038a12.

García-Prat L, Martínez-Vicente M, Perdiguero E, Ortet L, Rodríguez-Ubreva J, Rebollo E, Ruiz-Bonilla V, Gutarra S, Ballestar E, Serrano AL, Sandri M, Muñoz-Cánoves P (2016) Autophagy maintains stemness by preventing senescence. Nature 529: 37-42. DOI: 10.1038/nature16187.

Hocking LJ, Whitehouse C, Helfrich MH (2012) Autophagy: a new player in skeletal maintenance? Journal of Bone and Mineral Research: the Official Journal of the American Society for Bone and Mineral Research 27: 1439-1447. DOI: 10.1002/jbmr.1668.

Holmes D, Gawad S (2010) The application of microfluidics in biology. Methods in Molecular Biology (Clifton, N.J.) 583: 55-80. DOI: 10.1007/978-1-60327-106-6_2.

Inada M, Matsumoto C, Miyaura C (2011) Animal models for bone and joint disease. Ovariectomized and orchidectomized animals. Clinical Calcium 21: 164-170.

Jiang W, Li M, Chen Z, Leong KW (2016) Cell-laden microfluidic microgels for tissue regeneration. Lab on a Chip 16: 4482-4506. DOI: 10.1039/c6lc01193d.

Katt ME, Placone AL, Wong AD, Xu ZS, Searson PC (2016) In Vitro Tumor Models: Advantages, Disadvantages, Variables, and Selecting the Right Platform. Frontiers in Bioengineering and Biotechnology 4: 12. DOI: 10.3389/fbioe.2016.00012.

Kegelman CD, Mason DE, Dawahare JH, Horan DJ, Vigil GD, Howard SS, Robling AG, Bellido TM, Boerckel JD (2018) Skeletal cell YAP and TAZ combinatorially promote bone development. FASEB Journal: Official Publication of the Federation of American Societies for Experimental Biology 32: 2706-2721. DOI: 10.1096/fj.201700872R.

Lancaster MA, Renner M, Martin CA, Wenzel D, Bicknell LS, Hurles ME, Homfray T, Penninger JM, Jackson AP, Knoblich JA (2013) Cerebral organoids model human brain development and microcephaly. Nature 501: 373-379. DOI: 10.1038/nature12517.

Le Saux G, Wu MC, Toledo E, Chen YQ, Fan YJ, Kuo JC, Schvartzman M (2020) Cell-Cell Adhesion-Driven Contact Guidance and Its Effect on Human Mesenchymal Stem Cell Differentiation. ACS Applied Materials & Interfaces 12: 22399-22409. DOI: 10.1021/acsami.9b20939.

Li H, Li D, Ma Z, Qian Z, Kang X, Jin X, Li F, Wang X, Chen Q, Sun H, Wu S (2018) Defective autophagy in osteoblasts induces endoplasmic reticulum stress and causes remarkable bone loss. Autophagy 14: 1726-1741. DOI: 10.1080/15548627.2018.1483807.

Li J, Li X, Liu D, Hamamura K, Wan Q, Na S, Yokota H, Zhang P (2019) eIF2α signaling regulates autophagy of osteoblasts and the development of osteoclasts in OVX mice. Cell Death & Disease 10: 921. DOI: 10.1038/s41419-019-2159-z.

Li L, Yang S, Xu L, Li Y, Fu Y, Zhang H, Song J (2019) Nanotopography on titanium promotes osteogenesis via autophagy-mediated signaling between YAP and β-catenin. Acta Biomaterialia 96: 674-685. DOI: 10.1016/j.actbio.2019.07.007.

Ma C, Yu R, Li J, Chao J, Liu P (2023) Targeting proteostasis network in osteoporosis: Pathological mechanisms and therapeutic implications. Ageing Research Reviews 90: 102024. DOI: 10.1016/j.arr.2023.102024.

Ma Y, Qi M, An Y, Zhang L, Yang R, Doro DH, Liu W, Jin Y (2018) Autophagy controls mesenchymal stem cell properties and senescence during bone aging. Aging Cell 17: e12709. DOI: 10.1111/acel.12709.

Mansoorifar A, Gordon R, Bergan R, Bertassoni LE (2021) Bone-on-a-chip: microfluidic technologies and microphysiologic models of bone tissue. Advanced Functional Materials 31: 2006796. DOI: 10.1002/adfm.202006796.

Marsano A, Conficconi C, Lemme M, Occhetta P, Gaudiello E, Votta E, Cerino G, Redaelli A, Rasponi M (2016) Beating heart on a chip: a novel microfluidic platform to generate functional 3D cardiac microtissues. Lab on a Chip 16: 599-610. DOI: 10.1039/c5lc01356a.

Mizushima N, Komatsu M (2011) Autophagy: renovation of cells and tissues. Cell 147: 728-741. DOI: 10.1016/j.cell.2011.10.026.

Moya IM, Halder G (2019) Hippo-YAP/TAZ signalling in organ regeneration and regenerative medicine. Nature Reviews. Molecular Cell Biology 20: 211-226. DOI: 10.1038/s41580-018-0086-y.

Nelson MR, Ghoshal D, Mejías JC, Rubio DF, Keith E, Roy K (2021) A multi-niche microvascularized human bone marrow (hBM) on-a-chip elucidates key roles of the endosteal niche in hBM physiology. Biomaterials 270: 120683. DOI: 10.1016/j.biomaterials.2021.120683.

Onal M, Piemontese M, Xiong J, Wang Y, Han L, Ye S, Komatsu M, Selig M, Weinstein RS, Zhao H, Jilka RL, Almeida M, Manolagas SC, O'Brien CA (2013) Suppression of autophagy in osteocytes mimics skeletal aging. The Journal of Biological Chemistry 288: 17432-17440. DOI: 10.1074/jbc.M112.444190.

Paillat L, Coutant K, Dutilleul M, Le Lay S, Camus A (2023) Three-dimensional culture model to study the biology of vacuolated notochordal cells from mouse nucleus pulposus explants. European Cells & Materials 45: 72-87. DOI: 10.22203/eCM.v045a06.

Pan JX, Xiong L, Zhao K, Zeng P, Wang B, Tang FL, Sun D, Guo HH, Yang X, Cui S, Xia WF, Mei L, Xiong WC (2018) YAP promotes osteogenesis and suppresses adipogenic differentiation by regulating β-catenin signaling.

Bone Research 6: 18. DOI: 10.1038/s41413-018-0018-7.

Parfitt AM (1987) Trabecular bone architecture in the pathogenesis and prevention of fracture. The American Journal of Medicine 82: 68-72. DOI: 10.1016/0002-9343(87)90274-9.

Park SE, Georgescu A, Huh D (2019) Organoids-on-a-chip. Science (New York, N.Y.) 364: 960-965. DOI: 10.1126/science.aaw7894.

Pei T, Su G, Yang J, Gao W, Yang X, Zhang Y, Ren J, Shen Y, Liu X (2022) Fluid Shear Stress Regulates Osteogenic Differentiation via AnnexinA6-Mediated Autophagy in MC3T3-E1 Cells. International Journal of Molecular Sciences 23: 15702. DOI: 10.3390/ijms232415702.

Pinto V, Sousa P, Catarino SO, Correia-Neves M, Minas G (2017) Microfluidic immunosensor for rapid and highly-sensitive salivary cortisol quantification. Biosensors & Bioelectronics 90: 308-313. DOI: 10.1016/j.bios.2016.11.067.

Portillo-Lara R, Annabi N (2016) Microengineered cancer-on-a-chip platforms to study the metastatic microenvironment. Lab on a Chip 16: 4063-4081. DOI: 10.1039/c6lc00718j.

Qi D, Zhang K, Tian G, Jiang B, Huang Y (2021) Stretchable Electronics Based on PDMS Substrates. Advanced Materials (Deerfield Beach, Fla.) 33: e2003155. DOI: 10.1002/adma.202003155.

Reddi AH, Gay R, Gay S, Miller EJ (1977) Transitions in collagen types during matrix-induced cartilage, bone, and bone marrow formation. Proceedings of the National Academy of Sciences of the United States of America 74: 5589-5592. DOI: 10.1073/pnas.74.12.5589.

Remmers S, Mayer D, Melke J, Ito K, Hofmann S (2020) Measuring mineralised tissue formation and resorption in a human 3D osteoblast-osteoclast co-culture model. European Cells & Materials 40: 189-202. DOI: 10.22203/eCM.v040a12.

Salzer E, Schmitz TC, Mouser VH, Vernengo A, Gantenbein B, Jansen JU, Neidlinger-Wilke C, Wilke HJ, Grad S, Le Maitre CL, Tryfonidou MA, Ito K (2023) Ex vivo intervertebral disc cultures: degeneration-induction methods and their implications for clinical translation. European Cells & Materials 45: 88-112. DOI: 10.22203/eCM.v045a07.

Schapira D, Schapira C (1992) Osteoporosis: the evolution of a scientific term. Osteoporosis International: a Journal Established as Result of Cooperation between the European Foundation for Osteoporosis and the National Osteoporosis Foundation of the USA 2: 164-167. DOI: 10.1007/BF01623921.

Shihan MH, Kanwar M, Wang Y, Jackson EE, Faranda AP, Duncan MK (2020) Fibronectin has multifunctional roles in posterior capsular opacification (PCO). Matrix Biology: Journal of the International Society for Matrix Biology 90: 79-108. DOI: 10.1016/j.matbio.2020.02.004.

Shihan MH, Novo SG, Le Marchand SJ, Wang Y, Duncan MK (2021) A simple method for quantitating confocal fluorescent images. Biochemistry and Biophysics Reports 25: 100916. DOI: 10.1016/j.bbrep.2021.100916.

Smith LJ, Deymier AC, Boyle JJ, Li Z, Linderman SW, Pasteris JD, Xia Y, Genin GM, Thomopoulos S (2016) Tunability of collagen matrix mechanical properties via multiple modes of mineralization. Interface Focus 6: 20150070. DOI: 10.1098/rsfs.2015.0070.

Su G, Feng T, Pei T, Yang F, Sun D, Yu H, Wang X, Gao W, He J, Shen Y, Liu X (2021) Autophagy modulates FSS-induced epithelial-mesenchymal transition in hepatocellular carcinoma cells. Molecular Carcinogenesis 60: 607-619. DOI: 10.1002/mc.23327.

Su G, Zhang D, Li T, Pei T, Yang J, Tu S, Liu S, Ren J, Zhang Y, Duan M, Yang X, Shen Y, Zhou C, Xie J, Liu X (2023) Annexin A5 derived from matrix vesicles protects against osteoporotic bone loss via mineralization. Bone Research 11: 60. DOI: 10.1038/s41413-023-00290-9.

Théry M, Racine V, Piel M, Pépin A, Dimitrov A, Chen Y, Sibarita JB, Bornens M (2006) Anisotropy of cell adhesive microenvironment governs cell internal organization and orientation of polarity. Proceedings of the National Academy of Sciences of the United States of America 103: 19771-19776. DOI: 10.1073/pnas.0609267103.

Vimalraj S (2020) Alkaline phosphatase: Structure, expression and its function in bone mineralization. Gene 754: 144855. DOI: 10.1016/j.gene.2020.144855.

Wang X, Merkel M, Sutter LB, Erdemci-Tandogan G, Manning ML, Kasza KE (2020) Anisotropy links cell shapes to tissue flow during convergent extension. Proceedings of the National Academy of Sciences of the United States of America 117: 13541-13551. DOI: 10.1073/pnas.1916418117.

Wegst UGK, Bai H, Saiz E, Tomsia AP, Ritchie RO (2015) Bioinspired structural materials. Nature Materials 14: 23-36. DOI: 10.1038/nmat4089.

Whitesides GM (2006) The origins and the future of microfluidics. Nature 442: 368-373. DOI: 10.1038/nature05058.

Wilmer MJ, Ng CP, Lanz HL, Vulto P, Suter-Dick L, Masereeuw R (2016) Kidney-on-a-Chip Technology for Drug-Induced Nephrotoxicity Screening. Trends in Biotechnology 34: 156-170. DOI: 10.1016/j.tibtech.2015.11.001.

Wittkowske C, Reilly GC, Lacroix D, Perrault CM (2016) In Vitro Bone Cell Models: Impact of Fluid Shear Stress on Bone Formation. Frontiers in Bioengineering and Biotechnology 4: 87. DOI: 10.3389/fbioe.2016.00087.

Xiong J, Almeida M, O'Brien CA (2018) The YAP/TAZ transcriptional co-activators have opposing effects at different stages of osteoblast differentiation. Bone 112: 1-9. DOI: 10.1016/j.bone.2018.04.001.

Yang C, Tao H, Zhang H, Xia Y, Bai J, Ge G, Li W, Zhang W, Xiao L, Xu Y, Wang Z, Gu Y, Yang H, Liu Y,

Geng D (2022) TET2 regulates osteoclastogenesis by modulating autophagy in OVX-induced bone loss. Autophagy 18: 2817-2829. DOI: 10.1080/15548627.2022.2048432.

Yang J, Han Q, Li C, Yang H, Chen X, Wang X (2020) Circular RNA circ_0001105 Inhibits Progression and Metastasis of Osteosarcoma by Sponging miR-766 and Activating YTHDF2 Expression. OncoTargets and Therapy 13: 1723-1736. DOI: 10.2147/OTT.S234668.

Yang J, Pei T, Su G, Duan P, Liu X (2023) AnnexinA6: a potential therapeutic target gene for extracellular matrix mineralization. Frontiers in Cell and Developmental Biology 11: 1201200. DOI: 10.3389/fcell.2023.1201200.

Yu H, He J, Su G, Wang Y, Fang F, Yang W, Gu K, Fu N, Wang Y, Shen Y, Liu X (2021) Fluid shear stress activates YAP to promote epithelial-mesenchymal transition in hepatocellular carcinoma. Molecular Oncology 15: 3164-3183. DOI: 10.1002/1878-0261.13061.

Yu H, Hou Z, Chen N, Luo R, Yang L, Miao M, Ma X, Zhou L, He F, Shen Y, Liu X, Wang Y (2022) Yes-associated protein contributes to magnesium alloy-derivedinflammation in endothelial cells. Regenerative Biomaterials 9: rbac002. DOI: 10.1093/rb/rbac002.

Yu H, Hou Z, Xiang M, Yang F, Ma J, Yang L, Ma X, Zhou L, He F, Miao M, Liu X, Wang Y (2022) Arsenic trioxide activates yes-associated protein by lysophosphatidic acid metabolism to selectively induce apoptosis of vascular smooth muscle cells. Biochimica et Biophysica Acta. Molecular Cell Research 1869: 119211. DOI: 10.1016/j.bbamcr.2022.119211.

Zhang Y, Yu T, Ding J, Li Z (2023) Bone-on-a-chip platforms and integrated biosensors: Towards advanced in vitro bone models with real-time biosensing. Biosensors & Bioelectronics 219: 114798. DOI: 10.1016/j.bios.2022.114798.

Zhao B, Ye X, Yu J, Li L, Li W, Li S, Yu J, Lin JD, Wang CY, Chinnaiyan AM, Lai ZC, Guan KL (2008) TEAD mediates YAP-dependent gene induction and growth control. Genes & Development 22: 1962-1971. DOI: 10.1101/gad.1664408.

Zhou A, Yu H, Liu J, Zheng J, Jia Y, Wu B, Xiang L (2020) Role of Hippo-YAP Signaling in Osseointegration by Regulating Osteogenesis, Angiogenesis, and Osteoimmunology. Frontiers in Cell and Developmental Biology 8: 780. DOI: 10.3389/fcell.2020.00780.

Zhu Z, Tang T, He Z, Wang F, Chen H, Chen G, Zhou J, Liu S, Wang J, Tian W, Chen D, Wu X, Liu X, Zhou Z, Liu S (2023) Uniaxial cyclic stretch enhances osteogenic differentiation of OPLL-derived primary cells via YAP-Wnt/β-catenin axis. European Cells & Materials 45: 31-45. DOI: 10.22203/eCM.v045a03.

Editor's note: The Scientific Editor responsible for this paper was Chris Evans.